

Experimental realization of a two-dimensional synthetic spin-orbit coupling in ultracold Fermi gases

Lianghui Huang,¹ Zengming Meng,¹ Pengjun Wang,¹ Peng Peng,¹ Shao-Liang Zhang,² Liangchao Chen,¹ Donghao Li,¹ Qi Zhou^{†,2} and Jing Zhang^{†1,3}

¹State Key Laboratory of Quantum Optics and Quantum Optics Devices,
Institute of Opto-Electronics, Shanxi University, Taiyuan 030006, P.R.China

²Department of Physics, The Chinese University of Hong Kong, Shatin, New Territories, Hong Kong

³Synergetic Innovation Center of Quantum Information and Quantum Physics,
University of Science and Technology of China, Hefei, Anhui 230026, P. R. China

Spin-orbit coupling (SOC) is central to many physical phenomena, including fine structures of atomic spectra and quantum topological matters. Whereas SOC is in general fixed in a physical system, atom-laser interaction provides physicists a unique means to create and control synthetic SOC for ultracold atoms [1]. Though significant experimental progresses have been made [2–8], a bottleneck in current studies is the lack of a two-dimensional (2D) synthetic SOC, which is crucial for realizing high-dimensional topological matters. Here, we report the experimental realization of 2D SOC in ultracold ⁴⁰K Fermi gases using three lasers, each of which dresses one atomic hyperfine spin state. Through spin injection radio-frequency (rf) spectroscopy [4], we probe the spin-resolved energy dispersions of dressed atoms, and observe a highly controllable Dirac point created by the 2D SOC. Our work paves the way for exploring high-dimensional topological matters in ultracold atoms using Raman schemes.

There have been many theoretical proposals in the literature for creating multi-dimensional synthetic SOC [9–14], so that novel macroscopic quantum phenomena and quantum topological states could be studied using ultracold atoms [15–23]. Whereas these proposals have not been realized in laboratories, physicists have also just begun to explore topological phenomena with ultracold atoms in optical lattices [24–27]. Here we use the Raman scheme, to produce a highly controllable 2D synthetic SOC for an ultracold Fermi gas of ⁴⁰K. Such a SOC allows us to create and manipulate a stable Dirac point on a 2D plane, which is detected by spin injection rf spectroscopy [4].

We apply three far detuned lasers propagating on the $x - y$ plane to couple three ground hyperfine spin states, within the $4^2S_{1/2}$ ground electronic manifold, $|1\rangle = |F = 9/2, m_F = 3/2\rangle$, $|2\rangle = |F = 9/2, m_F = 1/2\rangle$ and $|3\rangle = |F = 7/2, m_F = 1/2\rangle$, where (F, m_F) are the quantum numbers for hyperfine spin states as shown in Fig. 1a, to the electronically excited states. Unlike the tripod scheme where a single excited state is considered [9–11, 15–18], in ⁴⁰K used here, the excited states include a fine-

structure doublet $4^2P_{1/2}$ (D_1 line) and $4^2P_{3/2}$ (D_2 line) with fine structure splitting of ~ 3.4 nm. Each of two D-line components additionally has hyperfine structures. New theoretical understandings are therefore required.

The microscopic Hamiltonian of our system can be written as

$$H = \sum_{i=1}^3 \left(\frac{\mathbf{p}^2}{2m} + \varepsilon_i \right) |i\rangle\langle i| + \sum_{j=1}^n E_j |j\rangle\langle j| + \sum_{i=1}^3 \left(\Omega_i e^{i(\mathbf{k}'_i \cdot \mathbf{r} + i\omega_i t + \theta_i)} \left(\sum_{j=1}^n M_{ji} |j\rangle\langle i| \right) + h.c. \right), \quad (1)$$

where \mathbf{p} denotes the momentum of atoms, \mathbf{k}'_i ($|\mathbf{k}'_i| = 2\pi/\lambda_i$) and ω_i are the wave vectors and frequencies of three lasers, Ω_i are the Rabi frequencies, i, j are the indices for the three ground hyperfine spin and the excited states respectively, ε_i and E_j are the ground and excited state energies, n is the total number of the excited states and M_{ij} is the matrix element of the dipole transition. Different from the proposal in reference [9, 10, 15], each hyperfine ground spin state here is dressed by one and only one laser field, regardless of the excited states it is coupled to. A gauge transformation, $|i\rangle \rightarrow e^{-i(\mathbf{k}'_i \cdot \mathbf{r} + \theta_i)} |i\rangle$, can be applied to eliminate the phase θ_i . All results discussed here are therefore insensitive to the phase difference, and the sophisticated and challenging phase lockings are no longer necessary.

Whereas the standard rotating wave approximation gets rid of the time dependence of the Hamiltonian, for the far detuned lasers, the excited states can be adiabatically eliminated, and the Hamiltonian is written as $H_a = p_z^2/(2m) + H_{xy}$,

$$H_{xy} = \sum_{i=1}^3 \left(\frac{(\mathbf{p} - \mathbf{k}_i)^2}{2m} + \delta_i \right) |i\rangle\langle i| - \sum_{i' \neq i} \frac{\Omega_{ii'}}{2} |i\rangle\langle i'|. \quad (2)$$

Here, δ_1 is set as zero (energy reference) for simplification, δ_2 (δ_3) corresponds to the two-photon Raman detuning between Raman laser 1 and 2 (1 and 3), and $\mathbf{k}_i = \hbar\mathbf{k}'_i$. All three $\Omega_{ii'} = \Omega_{i'i}$ are real, describing the Raman coupling strength between hyperfine ground states $|i\rangle \leftrightarrow |i'\rangle$. These values could be either derived from microscopic calculations (Supplementary Materials), or measured directly in our experiments [3]. The

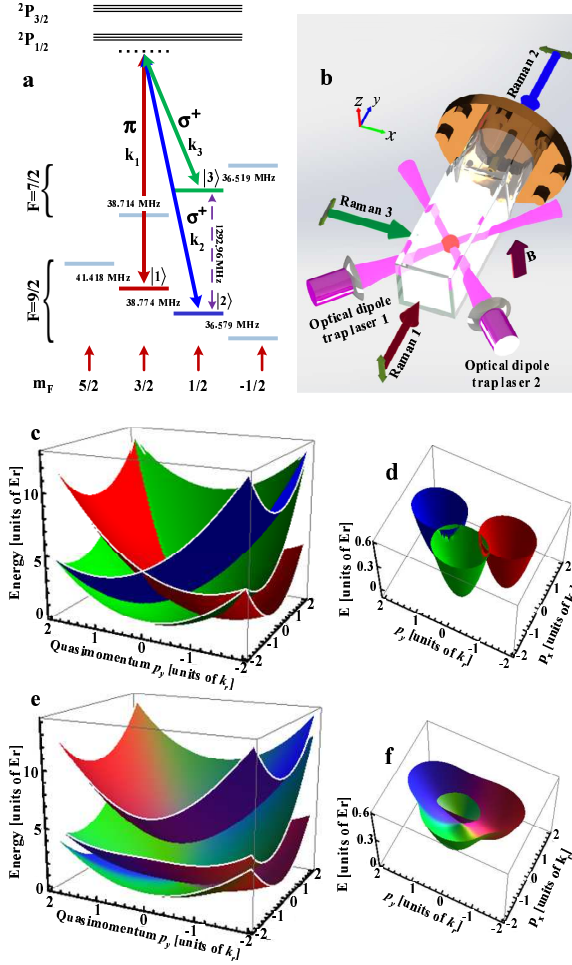


FIG. 1: Two-dimensional synthetic spin-orbit coupling. **a**, Schematic of energy levels of ^{40}K for creating 2D SOC. Each of the three Raman lasers dresses one hyperfine spin state from $|9/2, 3/2\rangle$ ($|1\rangle$), $|9/2, 1/2\rangle$ ($|2\rangle$) and $|7/2, 1/2\rangle$ ($|3\rangle$). Atoms are initially prepared in the free reservoir spin state $|9/2, 5/2\rangle$. **b**, The experimental geometry and the laser configuration. The Raman lasers 1 and 2 counter-propagate along the y axis and the Raman laser 3 propagates along the x axis, which are linearly polarized along z , x and y directions respectively. **c**, Energy-momentum dispersions in the absence of SOC ($\Omega_{12} = \Omega_{13} = \Omega_{23} = 0$). The three parabola are displaced from the origin by \mathbf{k}_i respectively in the (p_x, p_y) plane. **e**, Energy-momentum dispersions of three dressed states after turning on SOC ($-\Omega_{12} = 2\Omega_{13} = 2\Omega_{23} = E_r$), which show that the dispersions of two dressed states touch at a Dirac point. Here, $\delta_2 = \delta_3 = 0$. **d**, **f** are plots enlarging the low energy parts of **c** and **e**. In **e-f**, the weights of different hyperfine spin states in the dressed ones, the eigenstates of the Hamiltonian with SOC, are represented by assigning different colors to the hyperfine spin states. Red, blue and green represent $|1\rangle$, $|2\rangle$, and $|3\rangle$ respectively. The depth of each color indicates the percentage of the corresponding spin state in a dressed state.

single-photon recoil momentum $k_r = 2\pi\hbar/\lambda$ and recoil energy $E_r = k_r^2/2m$ are taken as natural momentum and energy units. Since the dispersion along the z direction is not affected by the lasers, we will focus on the 2D Hamiltonian H_{xy} .

Using the two lemmas in Supplementary Materials, we find out that a doubly degenerate point \mathbf{p}_0 exists in the momentum space, where \mathbf{p}_0 satisfies two independent equations

$$\begin{aligned} -\frac{(\mathbf{k}_1 - \mathbf{k}_2) \cdot \mathbf{p}_0}{m} + \delta_1 - \delta_2 &= -\frac{\Omega_{12}\Omega_{13}}{2\Omega_{23}} + \frac{\Omega_{12}\Omega_{23}}{2\Omega_{13}}, \\ -\frac{(\mathbf{k}_2 - \mathbf{k}_3) \cdot \mathbf{p}_0}{m} + \delta_2 - \delta_3 &= -\frac{\Omega_{12}\Omega_{23}}{2\Omega_{13}} + \frac{\Omega_{13}\Omega_{23}}{2\Omega_{12}} \end{aligned} \quad (3)$$

Defining the two dressed states with a touching point as a pseudo-spin-1/2, and projecting the Hamiltonian in equation (2) to this pseudo-spin-1/2 near the degenerate point \mathbf{p}_0 , an effective Hamiltonian at low energies can be obtained straightforwardly,

$$H_{SO} = (\lambda_{x1}p_x + \lambda_{y1}p_y)\sigma_x + (\lambda_{x2}p_x + \lambda_{y2}p_y)\sigma_z \quad (4)$$

where $p_{i=x,y} = p_i - p_{0,i}$. By rotating the momentum and the spin (see Supplementary Material), the Hamiltonian can be simplified as

$$H_{SO} = \lambda_x p'_x \sigma'_x + \lambda_y p'_y \sigma'_z, \quad (5)$$

where both λ_x and λ_y are finite. Equation (5) describes a 2D SOC, which is equivalent to the Dresselhaus coupling if a simple transformation $\sigma'_x \rightarrow \sigma'_y$, $\sigma'_z \rightarrow \sigma'_x$ is applied. Such a 2D SOC directly tells one that the doubly degenerate point at \mathbf{p}_0 corresponds to a Dirac point with a linear dispersion at low energies. In particular, both the amplitude and anisotropy λ_x/λ_y can be largely tuned (Supplementary Materials). As a demonstration, figures 1e (1f) and 1c (1d) show the comparison of the energy-momentum dispersion with and without SOC. The latter shows that energy dispersions of two dressed states touch at a Dirac point.

In this experiment, a homogeneous bias magnetic field $B_0 = 121.4$ G along the z axis (the gravity direction shown in Fig. 1b) produces a Zeeman shift to isolate these three hyperfine spin states from other ones in the Raman transitions, as shown in Fig. 1a. When three Raman lasers are nearly resonant with three ground states ($\delta_{i=1,2,3} \approx 0$), the nearest Raman transitions with other hyperfine states are $|7/2, 3/2\rangle \leftrightarrow |2\rangle$ and $|7/2, 3/2\rangle \leftrightarrow |3\rangle$, which have large two-photon Raman detunings about $h \times 60$ kHz. Thus we can neglect other hyperfine spin states and treat this system as a one with three ground nearly degenerate ground states.

As mentioned before, the Raman coupling strength $\Omega_{ii'}$ includes contributions from all excited states of two D-line components as shown in Fig. 2a and can be well tuned (Supplementary Materials). When the wavelength

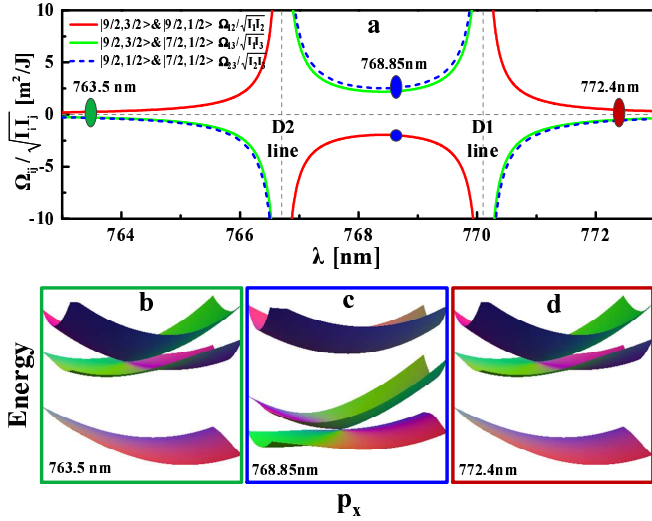


FIG. 2: **Controlling the Dirac point by changing the wavelength of the Raman lasers.** **a**, Red, green and blue curves represent the Raman coupling strength Ω_{12} , Ω_{13} and Ω_{23} as functions of the wavelength λ of the Raman lasers. Depending on λ , $\Omega_{12}\Omega_{13}\Omega_{23}$ can be either positive or negative. I_i is the intensity of the i th laser. **b-d**, The energy bands for the wavelength of 763.5 nm (blue-detuning D2 line), 768.85 nm (between D1 and D2 line) and 772.4 nm (red-detuning D1 line) respectively. The two higher dispersions touch at the Dirac point in **b** and **d** where $\Omega_{12}\Omega_{13}\Omega_{23}$ is positive. The two lower dispersions touch at the Dirac point in **c** where $\Omega_{12}\Omega_{13}\Omega_{23}$ is negative.

of the Raman lasers is larger than D_1 line (770.1 nm) or smaller than D_2 line (766.7 nm), $\Omega_{12}\Omega_{13}\Omega_{23} > 0$ (see the eigenvalues of dressed states in Supplementary Materials), and the Dirac point emerges in the highest two dressed states as shown in Figs. 2b and 2d. In contrast, when the wavelength of the Raman lasers is tuned between the D_1 line and D_2 line, $\Omega_{12}\Omega_{13}\Omega_{23} < 0$ and the Dirac point emerges when the lowest two dressed states become degenerate, as shown in Fig. 2c. This is quite different from the work [19], where only one excited state is considered and far blue-detuned lasers are used to make the degenerate dark states the low-lying ones in the manifold of ground electronic states.

We investigate the energy-momentum dispersions of three dressed states and the Dirac point by spin injection rf spectroscopy, which uses rf field to drive the atoms from a free spin-polarized state into an empty 2D SOC system. We start with a degenerate Fermi gas ^{40}K of 2×10^6 at the free reservoir spin state $|9/2, 5/2\rangle$ in a crossed optical dipole trap. A homogeneous bias magnetic field is ramped to $B_0 = 121.4$ G. Then three Raman lasers are ramped up in 60 ms from zero to its final value. Subsequently, a Gaussian shape pulse of the rf field is applied for 450 μs to drive atoms from the initial reservoir state $|9/2, 5/2\rangle$ to the final empty state with 2D SOC. rf field does not transfer momentum to the atoms and spin

injection occurs when the frequency of the rf matches the energy difference between the initial and final states. Since the spin state $|9/2, 5/2\rangle$ is coupled via rf to the state $|1\rangle$, rf spectroscopy also measures the weight of the $|1\rangle$ state, in addition to the energy dispersions with 2D SOC. Following the spin injection process, the Raman lasers, the optical trap and the magnetic field are switched off abruptly, and atoms freely expand for 12 ms in a magnetic field gradient applied along the x axis. Absorption image are taken along the z direction. By counting the number of atoms in state $|1\rangle$ as a function of the momentum and the rf frequency from the absorption image, we determine the energy band structure and locate the Dirac point.

Figure 3(a2) shows the momentum-resolved spin-injection spectrum when the one-photon detuning of the Raman lasers is set at the wavelength of 772.4 nm (red-detuning D1) and the corresponding theoretical plot is shown in Fig. 3(a1). The two higher energy dispersions touch at a Dirac point as shown in Fig. 3(a2). To further visualize the Dirac point, we plot the energy as a function of p_y for various p_x , as shown in Fig. 3(a3)-(a5). When the wavelength of the Raman lasers is tuned to 768.85 nm (between the D_1 line and D_2 line), two lower energy dispersions touch at a Dirac point, as shown in Fig. 3(b1)-(b5). These two wavelengths were used to investigate the 1D SOC [3, 5]. For the wavelength of the Raman lasers at 763.5 nm blue-detuning D2 line, we have observed that two higher energy dispersions touch at a Dirac point, similar to the 772.4 nm case. We also perform numerical calculations for the eigenvalues of the Hamiltonian in equation (2) and (5) according to experimental parameters and have found out a good agreement between theory and experiments.

The Dirac point created in this scheme is robust, in the sense that it moves in the momentum space without opening a gap when experimental parameters change. This comes from the fact that the Hamiltonian in equation (2) is real, and consequently, the SOC in equation (5) cannot contain the σ_y term. By modulating δ_i , Ω_i and \mathbf{k}_i , an arbitrary trajectory of the Dirac point in the momentum space can be designed in principle. As a demonstration, we fix the Raman detuning δ_2 and measure the positions of the Dirac point on the (p_x, p_y) plane as a function of δ_3 , as shown in Fig. 4a (blue dot). When fixing δ_3 and changing δ_2 , the Dirac point move along a different line. We also measure the energy at the Dirac point, as well as the energy separation ΔE from highest dressed state, as a function of the Raman coupling strength. Zero energy in Fig. 4b corresponds to the Zeeman energy splitting between $|9/2, 5/2\rangle$ and $|9/2, 3/2\rangle$. The energy of the Dirac point decreases and ΔE increases linearly with increasing the Raman coupling strength (inset of Fig. 4b).

In this work, we have realized a highly controllable 2D SOC and a stable Dirac point for ultracold fermionic atoms. In the future, we will develop technologies to

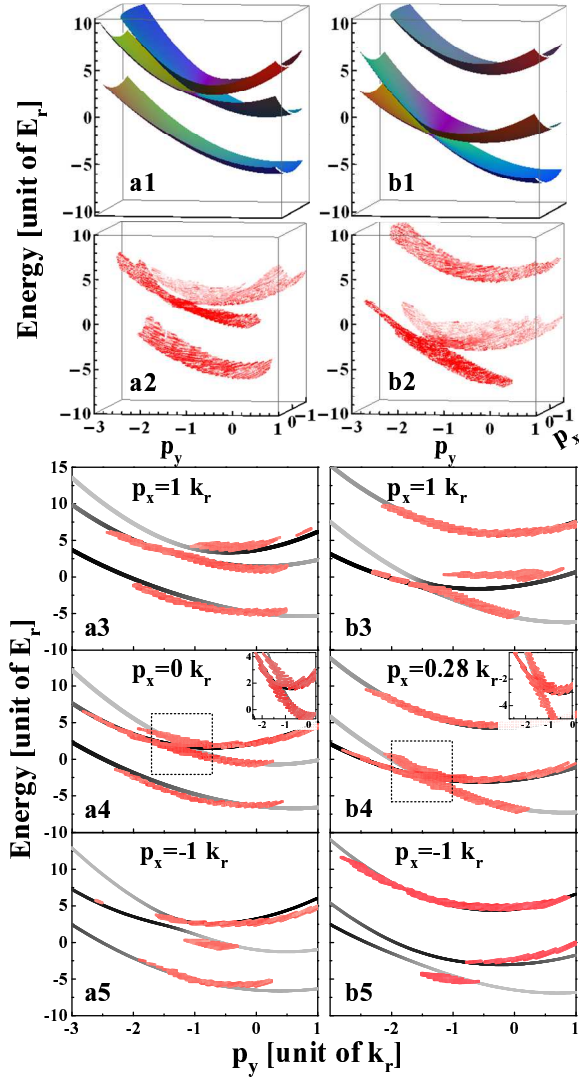


FIG. 3: The energy dispersions of dressed atoms measured by rf spin-injection spectroscopy. **a1-a7**, The one-photon detuning of the Raman lasers is set at the wavelength of 772.4 nm (red-detuning D_1). $\Omega_{12} = 3.58E_r$, $\Omega_{13} = -3.94E_r$, $\Omega_{23} = -4.66E_r$, $\delta_2 = -5.14E_r$, $\delta_3 = -3.23E_r$. **b1-b7**, The wavelength is set at 768.85 nm between the D_1 line and D_2 line. $\Omega_{12} = -4.96E_r$, $\Omega_{13} = 5.46E_r$, $\Omega_{23} = 6.46E_r$, $\delta_2 = -5.2E_r$, $\delta_3 = -2.13E_r$. **a1** and **b1** are the theoretical results using the realistic experimental parameters. **a2** and **b2** are experimental results measured by rf spin-injection spectroscopy. **a3-a5**, The cross-section drawings of (a1) and (a2) in the energy- p_y coordinates for different quasimomentum p_x . Red dots and solid curves are experimental and theoretical results respectively. The inset in **a4** is plot enlarging at Dirac point. Here, $\lambda_{x1} = 0$, $\lambda_{x2} = -0.42k_r/m$, $\lambda_{y1} = 1.5k_r/m$, and $\lambda_{y2} = -0.07k_r/m$ are obtained by the experimental parameters. **b3-b5**, The cross-section drawings of (b1) and (b2). The inset in **b4** is plot enlarging at Dirac point. $\lambda_{x,1}$, $\lambda_{x,2}$, $\lambda_{y,1}$ and $\lambda_{y,2}$ are the same as those in **a**, since Ω_{12}/Ω_{13} and Ω_{12}/Ω_{23} remain the same.

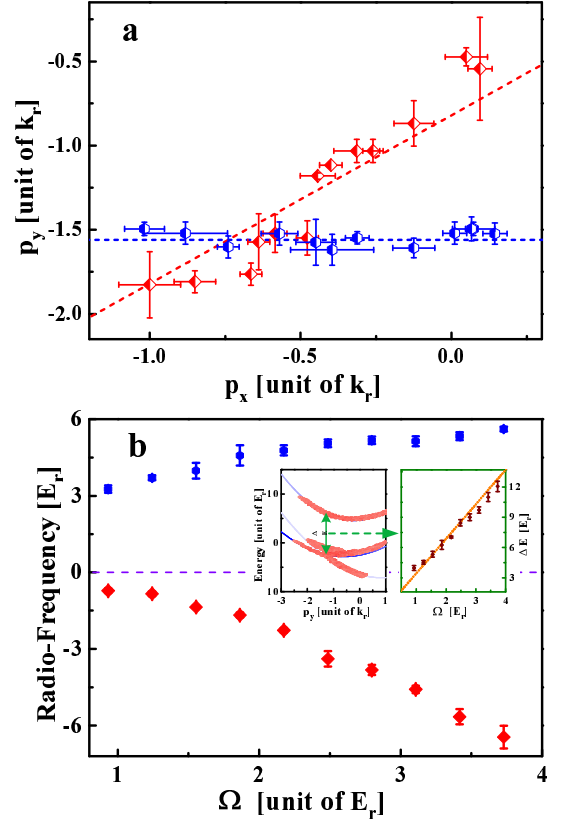


FIG. 4: Moving the Dirac point. **a**, controlling the Raman detuning δ_2 and δ_3 , the Dirac point moves along certain trajectories in the momentum space. Blue dots: δ_2 is fixed as $-5.45E_r$ and δ_3 is tuning at the range of $[-2E_r, 0.45E_r]$. Red dots: δ_3 is fixed as $-0.2E_r$ and δ_2 is tuning at the range of $[-7E_r, -2.5E_r]$. The other parameters are $\Omega_{12} = -4.96E_r$, $\Omega_{13} = 5.46E_r$, $\Omega_{23} = 6.46E_r$. **b**, the energy at the Dirac point and the corresponding energy of the highest dressed state with the same momentum \mathbf{p}_0 as a function of the Raman coupling strength. $-\Omega_{12} = 0.91\Omega_{13} = 0.77\Omega_{23} = \Omega$, $\delta_2 = -5.2E_r$ and $\delta_3 = -2.13E_r$. The left inset in **b** shows the energy dispersions, The right inset in **b** represents the energy separation ΔE between the Dirac point and the highest dressed state as a function of the Raman coupling strength. Here, the one-photon detuning of three Raman lasers is at the wavelength of 768.85 nm. The error bars represent the standard deviation of repeated measurements.

open and control the gap at the Dirac point to generate an effective perpendicular Zeeman field, so that interesting topological and other exotic superfluids will rise from s-wave interaction [20–23]. The heating effect due to spontaneous emission induced by Raman lasers is neglected here, since we inject atoms to states with SOC that are initially empty. Such a technical problem will become crucial if atoms are initially prepared in the states with 2D SOC. It may be overcome by using atomic species with the absence of the spontaneous emission, or by exploring the quantum quenching techniques so that topological properties may be extracted from quantum

dynamics in a relatively short time scale [29].

Method:

Experimental set-up. After sympathetic cooling with bosonic ^{87}Rb in a quadruple-Ioffe configuration magnetic trap, ^{40}K in the $|9/2, 9/2\rangle$ state and ^{87}Rb atoms in the $|2, 2\rangle$ are transferred into an optical dipole trap formed by two orthogonal 1064 nm laser beams. The Fermi gas is further evaporatively cooled to $T/T_F \approx 0.3$ about 2×10^6 ^{40}K with ^{87}Rb atoms in the optical trap [28], where T_F is the Fermi temperature defined by $T_F = (6N)^{1/3} \hbar \bar{\omega} / k_B$, and the geometric mean of trapping frequencies $\bar{\omega} \simeq 2\pi \times 80$ Hz in our system, N is the number of fermions. After removal of ^{87}Rb atoms, the fermionic atoms are transferred into the state $|9/2, 5/2\rangle$ via a rapid adiabatic passage induced by a rf field of 80 ms at 19.6 G. Here, the transition is addressed by a rf ramp that starts at 6.56 MHz to the end of 6.28 MHz. Then a homogeneous bias magnetic field along the z axis (gravity direction) is ramped to $B_0 = 121.4$ G by a pair of coils operating in the Helmholtz configuration.

Raman lasers. Three Raman lasers are derived from a CW Ti-sapphire single frequency laser. Two Raman beams 1 and 2 are frequency-shifted around $+201.144 \times 2$ MHz and $+220.531 \times 2$ MHz by two double-pass acousto-optic modulators (AOM), respectively. The Raman laser 3 is sent through two AOMs with double-pass and frequency-shifted -212.975×4 MHz. Then three Raman beams are coupled into three polarization maintaining single-mode fibers respectively in order to improve stability of the beam pointing and achieve better beam-profile quality. Behind the fibers, these three Raman beams have the maximum power 80 mW for each beam and they overlap in the atomic cloud with $1/e^2$ radii of 200 μm . The Raman lasers 1 and 2 counter-propagate along the y axis and the Raman laser 3 propagates along the x axis, which are linearly polarized along z , x and y directions respectively, corresponding to π , σ and σ polarization relative to the quantization axis z as shown in Fig. 1b.

[†]Corresponding author email: jzhang74@sxu.edu.cn, jzhang74@yahoo.com. [‡] qizhou@phy.cuhk.edu.hk.

We would like to thank Hui Zhai, Shizhong Zhang, Chuanwei Zhang, Han Pu and Hui Hu for helpful discussions. This research is supported by the National Basic Research Program of China (Grant No. 2011CB921601), NSFC (Grant No. 11234008, 11361161002, 11222430). QZ is supported by NSFC/RGC(NCUHK453/13).

-
- [1] Dalibard, J., Gerbier, F., Juzeliunas, G. & Öhberg, P. Artificial gauge potentials for neutral atoms. *Rev. Mod. Phys.* **83**, 1523 (2011).
 [2] Lin, Y.-J., Jiménez-García, K. & Spielman, I. B. Spin-orbit-coupled Bose-Einstein condensates. *Nature* **471**, 83-86 (2011).

- [3] Wang, P., Yu, Z., Fu, Z., Miao, J., Huang, L., Chai, S., Zhai, H. & Zhang, J. Spin-orbit coupled degenerate Fermi gases. *Phys. Rev. Lett.* **109**, 095301 (2012).
 [4] Cheuk, L. W. *et al.* Spin-injection spectroscopy of a spin-orbit coupled Fermi gas. *Phys. Rev. Lett.* **109**, 095302 (2012).
 [5] Williams, R. A., Beeler, M. C., LeBlanc, L. J. & Spielman I. B. Raman-induced interactions in a single-component Fermi gas near an s-wave Feshbach resonance. *Phys. Rev. Lett.* **111**, 095301 (2013).
 [6] Zhang, J.-Y. *et al.* Collective dipole oscillations of a spin-orbit coupled Bose-Einstein condensate. *Phys. Rev. Lett.* **109**, 115301 (2012).
 [7] Qu, C., Hammer, C., Gong, M., Zhang, C. & Engels, P. Observation of Zitterbewegung in a spin-orbit coupled Bose-Einstein condensates. *Phys. Rev. A* **88**, 021604(R) (2013).
 [8] Olson, A. J., Wang, S.-J., Niffenegger, R. J., Li, C. -H., Greene, C. H. & Chen, Y. P. Tunable Landau-Zener transitions in a spin-orbit-coupled Bose-Einstein condensate. *Phys. Rev. A* **90**, 013616 (2014).
 [9] Unanyan, R. G., Shore, B. W. & Bergmann, K. Laser-driven population transfer in four-level atoms: Consequences of non-abelian geometrical adiabatic phase factors. *Phys. Rev. A* **59**, 2910 (1999).
 [10] Ruseckas, J., Juzeliūnas, G., Öhberg, P. & Fleischhauer, M. Non-abelian gauge potentials for ultracold atoms with degenerate dark states. *Phys. Rev. Lett.* **95**, 010404 (2005).
 [11] Juzeliūnas, G., Ruseckas, J., Dalibard, & J. Generalized Rashba-Dresselhaus spin-orbit coupling for cold atoms. *Phys. Rev. A* **81**, 053403 (2010).
 [12] Campbell, D. L., Juzeliūnas, G. & Spielman, I. B. Realistic Rashba and Dresselhaus spin-orbit coupling for neutral atoms. *Phys. Rev. A* **84**, 025602 (2011).
 [13] Xu, Z. F., You, L. & Ueda, M. Atomic spin-orbit coupling synthesized with magnetic-field-gradient pulses. *Phys. Rev. A* **87**, 063634 (2013).
 [14] Anderson, B. M., Spielman, I. B. & Juzeliūnas, G. Magnetically generated spin-orbit coupling for ultracold atoms. *Phys. Rev. Lett.* **111**, 125301 (2013).
 [15] Stanescu, T. D., Zhang, C. & Galitski, V. Nonequilibrium spin dynamics in a trapped fermi gas with effective spin-orbit interactions. *Phys. Rev. Lett.* **99**, 110403 (2007).
 [16] Juzeliūnas, G., Ruseckas, J., Jacob, A., Santos, L. & Öhberg, P. Double and negative reflection of cold atoms in non-Abelian gauge potentials. *Phys. Rev. Lett.* **100**, 200405 (2008).
 [17] Vaishnav, J. Y. & Clark, C. W. Observing Zitterbewegung with ultracold atoms. *Phys. Rev. Lett.* **100**, 153002 (2008).
 [18] Larson, J. & Sjöqvist, E. Jahn-Teller-induced Berry phase in spin-orbit-coupled Bose-Einstein condensates. *Phys. Rev. A* **79**, 043627 (2009).
 [19] Zhang, Y., Mao, L. & Zhang, C. Mean-field dynamics of spin-orbit coupled Bose-Einstein condensates. *Phys. Rev. Lett.* **108**, 035302 (2012).
 [20] Zhang, C. Spin-orbit coupling and perpendicular Zeeman field for fermionic cold atoms: Observation of the intrinsic anomalous Hall effect. *Phys. Rev. A* **82**, 021607(R) (2010).
 [21] Zhu, S. -L., Shao, L. -B., Wang, Z. D. & Duan, L. -M. Probing non-Abelian statistics of Majorana Fermions in ultracold atomic superfluid. *Phys. Rev. Lett.* **106**, 100404 (2011).
 [22] Hu, H., Jiang, L., Liu, X. -J. & Han, P. Prob-

- ing anisotropic superfluidity in atomic Fermi gases with Rashba spin-orbit coupling. *Phys. Rev. Lett.* **107**, 195304 (2011).
- [23] Yu, Z. -Q. & Zhai, H. Spin-orbit coupled Fermi gases across a Feshbach resonance. *Phys. Rev. Lett.* **107**, 195305 (2011).
- [24] Tarruell, L., Greif, D., Uehlinger, T., Jotzu, G. & Esslinger, T. Creating, moving and merging Dirac points with a Fermi gas in a tunable honeycomb lattice. *Nature* **483**, 302 (2012).
- [25] Jotzu, G., Messer, M., Desbuquois, R., Lebrat, M., Uehlinger, T., Greif, D. & Esslinger, T. Experimental realization of the topological Haldane model with ultracold fermions. *Nature* **515**, 237 (2014).
- [26] Aidelsburger, M., Atala, M., Lohse, M., Barreiro, J. T., Paredes, B. & Bloch, I. Realization of the Hofstadter Hamiltonian with ultracold atoms in optical lattices. *Phys. Rev. Lett.* **111**, 185301 (2013).
- [27] Miyake, H., Siviloglou, G. A., Kennedy, C. J., Burton, W. C. & Ketterle, W. Realizing the Harper Hamiltonian with laser-assisted tunneling in optical lattices. *Phys. Rev. Lett.* **111**, 185302 (2013).
- [28] Xiong, D. *et al.* Quantum degenerate Fermi-Bose mixtures of ^{40}K and ^{87}Rb atoms in a quadrupole-Ioffe configuration trap. *Chin. Phys. Lett.* **25**, 843 (2008).
- [29] Setiawan, F., Sengupta, K., Spielman, I. B., & Sau, J. D. Dynamical detection of a topological phase transition in one-dimensional spin-orbit-coupled Fermi gases. arXiv:1503.07167
- [30] Our supplementary materials.

SUPPLEMENTARY MATERIAL

2D synthetic SOC and the Dirac point

Despite its simple form, equation (2) in the main text leads to significant results of a highly controllable Dirac point and a 2D synthetic SOC. To see this fact, we first present two lemmas.

Lemma 1, a real 3×3 matrix

$$\begin{pmatrix} -\frac{\Omega_{12}\Omega_{13}}{2\Omega_{23}} & -\frac{\Omega_{12}}{2} & -\frac{\Omega_{13}}{2} \\ -\frac{\Omega_{12}}{2} & -\frac{\Omega_{12}\Omega_{23}}{2\Omega_{13}} & -\frac{\Omega_{23}}{2} \\ -\frac{\Omega_{13}}{2} & -\frac{\Omega_{23}}{2} & -\frac{\Omega_{13}\Omega_{23}}{2\Omega_{12}} \end{pmatrix}, \quad (6)$$

has two degenerate eigenstates $|A\rangle$ and $|B\rangle$ with zero eigenenergy $E_A = E_B = 0$,

$$\begin{aligned} |A\rangle &= \frac{1}{N_1} \left(-\Omega_{23}|1\rangle + \Omega_{13}|2\rangle \right) \\ |B\rangle &= \frac{1}{N_2} \left(\Omega_{13}|1\rangle + \Omega_{23}|2\rangle - \frac{\Omega_{12}(\Omega_{13}^2 + \Omega_{23}^2)}{\Omega_{13}\Omega_{23}}|3\rangle \right) \end{aligned} \quad (7)$$

where $N_1 = \sqrt{\Omega_{13}^2 + \Omega_{23}^2}$ and $N_2 = \sqrt{\Omega_{13}^2 + \Omega_{23}^2 + \frac{\Omega_{12}^2(\Omega_{13}^2 + \Omega_{23}^2)^2}{\Omega_{13}^2\Omega_{23}^2}}$ are the normalization factors. The third eigenstate $|C\rangle$ has the energy

$$E_C = -\frac{1}{2\Omega_{12}\Omega_{13}\Omega_{23}}(\Omega_{12}^2\Omega_{13}^2 + \Omega_{12}^2\Omega_{23}^2 + \Omega_{13}^2\Omega_{23}^2). \quad (8)$$

For positive and negative $\Omega_{12}\Omega_{13}\Omega_{23}$, $|C\rangle$ is the ground or excited state respectively.

Lemma 2, there always exist a finite \mathbf{p}_0 to satisfy a set of three equations

$$\frac{(\mathbf{p}_0 - \mathbf{k}_i)^2}{2m} + \delta_i = \epsilon - \frac{\Omega_{ii'}\Omega_{ii''}}{2\Omega_{i'i''}}, \quad i = 1, 2, 3 \quad (9)$$

where ϵ is a constant, $i \neq i' \neq i''$, provided that $\Omega_{ii'} \neq 0$ for any i, i' , and none of these three momenta $\mathbf{k}_i = \hbar\mathbf{k}'_i$ is parallel to other ones so that the momenta $\mathbf{k}_1 - \mathbf{k}_2$, $\mathbf{k}_2 - \mathbf{k}_3$, and $\mathbf{k}_1 - \mathbf{k}_3$, two of which are independent, could span a plane.

These three equations are equivalent to

$$-\frac{\mathbf{p}_0}{m} \cdot (\mathbf{k}_1 - \mathbf{k}_2) + (\delta_1 - \delta_2) = -\frac{\Omega_{12}\Omega_{13}}{2\Omega_{23}} + \frac{\Omega_{12}\Omega_{23}}{2\Omega_{13}} \quad (10)$$

$$-\frac{\mathbf{p}_0}{m} \cdot (\mathbf{k}_2 - \mathbf{k}_3) + (\delta_2 - \delta_3) = -\frac{\Omega_{12}\Omega_{23}}{2\Omega_{13}} + \frac{\Omega_{13}\Omega_{23}}{2\Omega_{12}} \quad (11)$$

$$-\frac{\mathbf{p}_0}{m} \cdot (\mathbf{k}_3 - \mathbf{k}_1) + (\delta_3 - \delta_1) = -\frac{\Omega_{13}\Omega_{23}}{2\Omega_{12}} + \frac{\Omega_{12}\Omega_{13}}{2\Omega_{23}}, \quad (12)$$

only two of which are independent, since the summation of all three become zero on both sides of the equation. Thus it is sufficient to consider only the first two equations.

If the two momenta $\mathbf{k}_1 - \mathbf{k}_2$ and $\mathbf{k}_2 - \mathbf{k}_3$ are not parallel to each other, they span a plane. Define this plane as the $x - y$ plane, the z -component of \mathbf{p}_0 drops off from these equations, and we could consider a two-dimensional problem. The solutions of equations 10 and 11 form two lines on this plane. The intersection then uniquely determines the location of \mathbf{p}_0 on this plane, and the corresponding energy of this degenerate point is ϵ . Note that regardless of the microscopic parameters, there is always a trivial solution of \mathbf{p}_0 at infinity, which is irrelevant to our discussions here.

Project the Hamiltonian to the subspace of $|A\rangle$ and $|B\rangle$, the effective Hamiltonian is,

$$H_e = \begin{pmatrix} \langle A|H|A\rangle & \langle A|H|B\rangle \\ \langle B|H|A\rangle & \langle B|H|B\rangle \end{pmatrix} = \begin{pmatrix} \frac{1}{N_1^2}(\Omega_{23}^2\epsilon_{1\mathbf{p}} + \Omega_{13}^2\epsilon_{2\mathbf{p}}) & \frac{1}{N_1N_2}(\epsilon_{2\mathbf{p}} - \epsilon_{1\mathbf{p}})\Omega_{13}\Omega_{23} \\ \frac{1}{N_1N_2}(\epsilon_{2\mathbf{p}} - \epsilon_{1\mathbf{p}})\Omega_{13}\Omega_{23} & \frac{1}{N_2^2}\left(\Omega_{23}^2\epsilon_{1\mathbf{p}} + \Omega_{13}^2\epsilon_{2\mathbf{p}} + \frac{\Omega_{12}^2(\Omega_{13}^2 + \Omega_{23}^2)^2}{\Omega_{13}^2\Omega_{23}^2}\epsilon_{3\mathbf{p}}\right) \end{pmatrix} \quad (13)$$

where $\epsilon_{i\mathbf{p}} = (\mathbf{p} - \mathbf{k}_i)^2/(2m) + \delta_i$. Expand H_e near the degenerate point \mathbf{p}_0 , and redefine $\mathbf{p} = \mathbf{p} - \mathbf{p}_0$, and $\mathbf{k}_i = \mathbf{k}_i - \mathbf{p}_0$, then the effective Hamiltonian can be written as:

$$H_e = \begin{pmatrix} \frac{1}{mN_1^2}(\Omega_{23}^2\mathbf{k}_1 + \Omega_{13}^2\mathbf{k}_2) \cdot \mathbf{p} & \frac{1}{mN_1N_2}\Omega_{13}\Omega_{23}(\mathbf{k}_1 - \mathbf{k}_2) \cdot \mathbf{p} \\ \frac{1}{mN_1N_2}\Omega_{13}\Omega_{23}(\mathbf{k}_1 - \mathbf{k}_2) \cdot \mathbf{p} & \frac{1}{mN_2^2}\left(\Omega_{23}^2\mathbf{k}_1 + \Omega_{13}^2\mathbf{k}_2 + \frac{\Omega_{12}^2(\Omega_{13}^2 + \Omega_{23}^2)^2}{\Omega_{13}^2\Omega_{23}^2}\mathbf{k}_3\right) \cdot \mathbf{p} \end{pmatrix} + \epsilon \cdot I_{2 \times 2} \quad (14)$$

where $I_{2 \times 2}$ is the identity matrix.

Dropping the terms that are independent on spin, H_e can be in general written as

$$H_e = (\lambda_{x1}p_x + \lambda_{y1}p_y)\sigma_x + (\lambda_{x2}p_x + \lambda_{y2}p_y)\sigma_z \quad (15)$$

where the coefficients λ_{x1} , λ_{x2} , λ_{y1} , λ_{y2} depend on the microscopic parameters such as \mathbf{k}_i and $\Omega_{ii'}$.

To simplify the notations, we chose a coordinate so that $k_{1y} = k_{2y}$. Then the effective Hamiltonian (14) can be written as

$$H_e = ap_x\sigma_x + bp_x\sigma_z + cp_y\sigma_z + \epsilon I \quad (16)$$

where a , b , c and ϵ are all constant:

$$\begin{aligned} a &= \frac{1}{mN_1N_2}\Omega_{13}\Omega_{23}(k_{1x} - k_{2x}) \\ b &= \frac{1}{2mN_1^2}(\Omega_{23}^2k_{1x} + \Omega_{13}^2k_{2x}) - \frac{1}{2mN_2^2}\left(\Omega_{23}^2k_{1x} + \Omega_{13}^2k_{2x} + \frac{\Omega_{12}^2(\Omega_{13}^2 + \Omega_{23}^2)^2}{\Omega_{13}^2\Omega_{23}^2}k_{3x}\right) \\ c &= \frac{1}{2mN_1^2}(\Omega_{23}^2k_{1y} + \Omega_{13}^2k_{2y}) - \frac{1}{2mN_2^2}\left(\Omega_{23}^2k_{1y} + \Omega_{13}^2k_{2y} + \frac{\Omega_{12}^2(\Omega_{13}^2 + \Omega_{23}^2)^2}{\Omega_{13}^2\Omega_{23}^2}k_{3y}\right) = \frac{\Omega_{12}^2(\Omega_{13}^2 + \Omega_{23}^2)^2}{2mN_2^2\Omega_{13}^2\Omega_{23}^2}(k_{1y} - k_{3y}) \end{aligned}$$

When $(\mathbf{k}_1 - \mathbf{k}_2) \times (\mathbf{k}_1 - \mathbf{k}_3) \neq 0$, $a \neq 0$ and $c \neq 0$ are satisfied.

We rotate \mathbf{p} about the p_z axis by φ and the spin about the σ_y axis by θ . If φ and θ satisfy

$$(a^2 + b^2 - c^2)\sin 2\varphi + 2bc\cos 2\varphi = 0, \quad (a^2 - b^2 - c^2)\sin 4\theta + 2ab\cos 4\theta = 0, \quad (17)$$

the effective Hamiltonian is simplified as

$$H_{SO} = \lambda_x p'_x \sigma'_x + \lambda_y p'_y \sigma'_z, \quad (18)$$

where

$$\begin{aligned} \lambda_x &= a \cos \varphi \cos 2\theta - b \cos \varphi \sin 2\theta + c \sin \varphi \sin 2\theta \\ \lambda_y &= a \sin \varphi \sin 2\theta + b \sin \varphi \cos 2\theta + c \cos \varphi \cos 2\theta \end{aligned} \quad (19)$$

A special case is a perfect symmetric configuration, $\delta_1 = \delta_2 = \delta_3$, $\Omega_{12} = \Omega_{13} = \Omega_{23}$ so that \mathbf{k}_i form an equilateral triangle. The Hamiltonian is $H_{SO} = \frac{d}{2\sqrt{3}m}(p_x\sigma_x + p_y\sigma_z)$ where $d = |\mathbf{k}_i - \mathbf{k}_j|$.

Calculation of Raman coupling strength

The Raman coupling strength can be expressed as [1]

$$\Omega_{ij} = -\frac{I_0}{\hbar^2 c \epsilon_0} \sum_{F'', m_F''} \frac{\langle F^j, m_F^j | e r_q | F'', m_F'' \rangle \langle F'', m_F'' | e r_q | F^i, m_F^i \rangle}{\Delta}, \quad (20)$$

where, $I_0 = \sqrt{I_1 \cdot I_2}$, and the I_i is the intensity of each Raman laser light. c is the speed of light, ϵ_0 is the permittivity of vacuum, e is the elementary charge, and q is an index labeling the component of r in the spherical basis. Δ is one-photon detuning of Raman lasers. $|F^i, m_F^i\rangle$ and $|F^j, m_F^j\rangle$ are two ground hyperfine spin states coupled by a pair of Raman laser. $|F'', m_F''\rangle$ is the middle excited hyperfine spin state in the Raman process.

Here, we consider ^{40}K atoms, the excited states of the laser-atom coupling involve a fine-structure doublet $4^2P_{1/2}$ (D_1 line) and $4^2P_{3/2}$ (D_2 line) with fine structure splitting of ~ 3.4 nm as shown in Fig. 5. The Raman coupling strength can be written with two contributions from D_1 line and D_2 line [2],

$$\begin{aligned} \Omega_{ij} = & -\frac{I_0}{\hbar^2 c \epsilon_0} \left[\frac{1}{\Delta_{D1}} \times \sum_{F_1'', m_F''} \langle F^j, m_F^j | e r_q | F_1'', m_F'' \rangle \langle F_1'', m_F'' | e r_q | F^i, m_F^i \rangle \right. \\ & \left. + \frac{1}{\Delta_{D2}} \times \sum_{F_2'', m_F''} \langle F^j, m_F^j | e r_q | F_2'', m_F'' \rangle \langle F_2'', m_F'' | e r_q | F^i, m_F^i \rangle \right]. \end{aligned} \quad (21)$$

Here, Δ_{D1} and Δ_{D2} are one-photon detuning of Raman lasers relative to the D_1 and D_2 line respectively. It is required in here that Δ_{D1} and Δ_{D2} are very larger than the hyperfine energy splitting of the excited state.

The Raman coupling strength for D_1 and D_2 line can be simplified as

$$\begin{aligned} \Omega_{ij}^{D1, (F'', m_F'')} = & -\frac{I_0}{\hbar^2 c \epsilon_0} \frac{\langle F^j, m_F^j | e r_q | F'', m_F'' \rangle \langle F'', m_F'' | e r_q | F^i, m_F^i \rangle}{\Delta_{D1}} \\ = & -\frac{I_0}{\hbar^2 c \epsilon_0} \frac{C_i^{(F'', m_F'')} \cdot C_j^{(F'', m_F'')}}{\Delta_{D1}} \langle J = 1/2 | e r_q | J'' = 1/2 \rangle^2, \end{aligned} \quad (22)$$

$$\begin{aligned} \Omega_{ij}^{D2, (F'', m_F'')} = & -\frac{I_0}{\hbar^2 c \epsilon_0} \frac{\langle F^j, m_F^j | e r_q | F'', m_F'' \rangle \langle F'', m_F'' | e r_q | F^i, m_F^i \rangle}{\Delta_{D2}} \\ = & -\frac{I_0}{\hbar^2 c \epsilon_0} \frac{C_i^{(F'', m_F'')} \cdot C_j^{(F'', m_F'')}}{\Delta_{D2}} \langle J = 1/2 | e r_q | J'' = 3/2 \rangle^2. \end{aligned} \quad (23)$$

Here, $C_i^{(F'', m_F'')}$ is the hyperfine dipole matrix element between the ground $|F^i, m_F^i\rangle$ and the excited hyperfine state $|F'', m_F''\rangle$ depending on π or σ^\pm transition, and $\langle J = 1/2 | e r_q | J'' = 1/2 \rangle$ and $\langle J = 1/2 | e r_q | J'' = 3/2 \rangle$ are the $D1$ and $D2$ transition dipole matrix element respectively, whose values all can be found in [3]. Therefore, the Raman coupling strength Ω_{12} , Ω_{13} and Ω_{23} as a function of one-photon detuning can be obtained from summing contributions from all the excited hyperfine states of two D-line components using Eqs. 21-23, as shown in Fig. 2a in the main text.

[1] T. A. Savard, S. R. Granade, K. M. O'Hara, M. E. Gehm, and J. E. Thomas, Phys. Rev. A **60**, 4788 (1999).

[2] L. Huang, P. Wang, Z. Fu, and J. Zhang, Acta Optica Sinica. **34**(7), 0727002 (2014).

[3] The data of ^{40}K can be from T. Tiecke, Ph.D. thesis, University of Amsterdam, 2010. The similar data of ^{87}Rb is from D. A. Steck, <http://steck.us/alkalidata>.

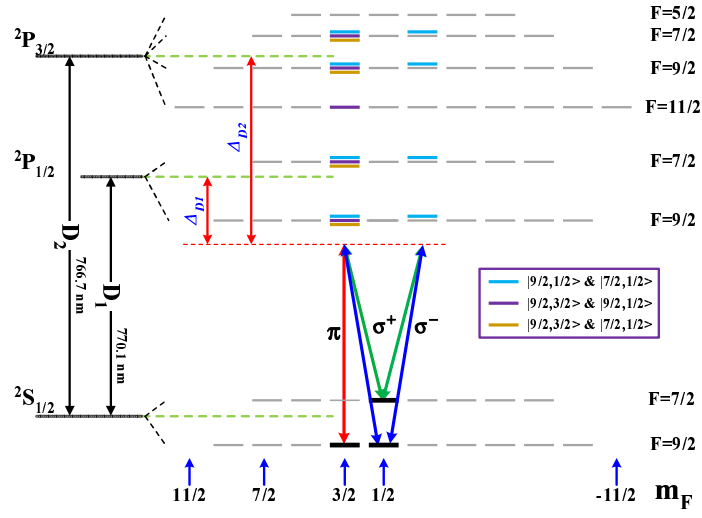


FIG. 5: (Color online). Schematic of energy levels of ^{40}K .